Article

The Cyclic Stability of the Superelasticity in Quenched and Aged $Ni_{44}Fe_{19}Ga_{27}Co_{10}$ Single Crystals

Ekaterina Timofeeva *, Elena Panchenko, Maria Zherdeva, Aida Tokhmetova and Yuriy I. Chumlyakov *

Laboratory for Physics of High-Strength Crystals, Siberian Physical-Technical Institute, National Research Tomsk State University, Lenina Str. 36, 634050 Tomsk, Russia; panchenko@mail.tsu.ru (E.P.); zhmv@mail.tsu.ru (M.Z.); aida.tokhmetova@mail.tsu.ru (A.T.)

* Correspondence: katie@mail.tsu.ru (E.T.); chum@phys.tsu.ru (Y.I.C.)

Abstract: The effect of aging (at 773 K for 1 h) on the cyclic stability of superelasticity was studied in preliminarily quenched (after annealing at 1448 K for 1 h) $Ni_{44}Fe_{19}Ga_{27}Co_{10}$ [001]-oriented single crystals. It was shown that NiFeGaCo single crystals (both quenched and aged) exhibited highly stable superelasticity during more than 10^5 loading/unloading cycles in compression without destruction. The degradation of the superelasticity curves was divided into stages, and each stage of degradation was carefully considered. The precipitation of ω-phase particles led to a change in the degradation mechanism of superelasticity in the aged crystals. The main degradation mechanism for quenched crystals is a formation of uniform distribution of dislocations; for aged crystals, the microstructural degradation mechanisms consist of a non-uniform distribution of dislocations around the particles and the appearance of residual martensite.

Keywords: cyclic stability; superelasticity; single crystals; martensitic transformations; critical stress; stress hysteresis; aging

1. Introduction

The Heusler NiFeGaCo alloy is one of the promising shape memory alloys. These alloys demonstrate multistage thermoelastic martensitic transformations (MT) from $B2(L2_1)$-austenite to $L1_0$-martensite through modulated 10M(14M)-phases [1]. Such effects, such as superelasticity (SE) and shape memory effect (SME), are observed on the basis of MT. SE is observed during loading/unloading cycles and is characterized by significant inelastic strain. The given inelastic strain is recovered during unloading. NiFeGaCo single crystals with cobalt content ranging from 0 to 6% are characterized by a wide SE temperature range, large reversible strain, narrow stress hysteresis, and high cyclic stability of SE (up to 5×10^4 cycles) [2–6].

Recent studies [7,8] have shown that increasing the cobalt content above 10% led to a strain glass transition in these materials, as in numerous other materials that deviate from stoichiometric compositions and contain a large number of point defects [9,10]. These defects impede the thermal-induced MT but contribute to strain glass transitions from unfrozen strain glass into frozen strain glass during stress-free cooling [7–9]. Such materials are characterized by the absence of thermal-induced transitions, high strength properties, high resistance of the matrix to forming stress-induced martensite, and narrow stress hysteresis. However, strain glass alloys have been poorly studied, especially NiFeGaCo alloys with a cobalt content $C_{Co} \geq 10\%$. Only a few studies of NiFeGaCo alloys with $C_{Co} \geq 10\%$ present their significant scientific potential [7,8,11,12]. NiFeGaCo alloys with a cobalt content of 10% are of interest because they still undergo thermal-induced MT but are characterized by typical features for strain glass transitions, such as a logarithmic dependence of temperature curves of the elastic modulus E(T) and internal friction tanδ(T) on frequency [13].

The design of NiFeGaCo shape memory alloys includes studying their cyclic stability, the degradation mechanisms of SE, and creating methods for increasing their resistance to cyclic tests. For example, applying shape memory alloys as sensors, dampers, and actuators requires 10^4 loading/unloading cycles, whereas their application in thermal valves, clamps, and micropincers requires at least 10^5 cooling/heating cycles with stable properties [14]. As for studies on SE cyclic stability in NiFeGaCo alloys, there are a few works [4,6,7] that did not clarify the microstructural mechanisms of degradation for NiFeGaCo alloys. Moreover, the number of cycles in these studies did not exceed 5×10^4 cycles [6]. Therefore, the conclusions of these studies are insufficient to predict the dependence of the SE parameters on the higher number of cycles. Single crystals of NiFeGaCo alloys are more promising for further investigation of the SE cyclic stability during large numbers of cycles, up to 10^5.

The main aspect of the present study is the high cobalt content of 10 at.%. First, the higher cobalt content can cause higher ductility in the material. As shown in our previous work [11], an increase in the cobalt content of up to 15% resulted in weak cyclic stability and increased fragility. The $Ni_{39}Fe_{19}Ga_{27}Co_{15}$ single crystals were destroyed during the first 30–50 cycles. In contrast, the $Ni_{44}Fe_{19}Ga_{27}Co_{10}$ alloy was not destroyed and was weakly degraded over 500 loading/unloading cycles. However, 500 loading/unloading cycles were insufficient to examine cyclic stability and determine the degradation mechanisms of these materials. Second, the increase in cobalt content from 6 to more than 10% led to a change in the crystal lattice of the secondary phase particles (from γ' to ω) [7,11]. Therefore, the study of the effect of ω-phase particles on SE cyclic stability in $Ni_{44}Fe_{19}Ga_{27}Co_{10}$ single crystals is relevant. Choosing a different composition and a different crystal structure of the secondary phase in comparison with the literature allows us to find a commonality of the degradation mechanisms for NiFeGaCo alloys, regardless of the cobalt content and the crystal structure of the secondary phase. Therefore, the aim of this work was to study SE cyclic stability (during 10^5 loading/unloading cycles) in quenched $Ni_{44}Fe_{19}Ga_{27}Co_{10}$ crystals without particles and in aged $Ni_{44}Fe_{19}Ga_{27}Co_{10}$ crystals containing ω-phase particles to clarify the effect of ω-phase particles on SE cyclic stability and to establish the microstructural mechanisms of degradation in heterophase NiFeGaCo alloys.

2. Materials and Methods

These studies were conducted only on single crystals because of the extreme brittleness of NiFeGaCo polycrystals. The high-strength [001]-orientation was chosen for the study. The Bridgman method [15,16] was used to grow the $Ni_{44}Fe_{19}Ga_{27}Co_{10}$ (at.%) single crystals. Single crystal growth was performed on a special installation in a ceramic crucible in an inert He atmosphere. The Bridgman method concludes with the heating of the polycrystal above the melting point and follows with slow cooling. Cooling was started from one end of the crucible, where a single crystal of one crystallographic orientation was grown on the seed along the length of the crucible. The formation of single crystals was confirmed by X-ray diffraction analysis, optical and electron microscopy.

These studies were conducted on single crystals after two thermal treatments. First, samples were annealed at 1448 K for 1 h with subsequent water quenching (quenched crystals). Then, one part of the quenched samples was aged at 773 K for 1 h, followed by quenching (aged crystals). For annealing or aging, the samples in a quartz tube filled with argon were put in a hot area of the furnace (Carbolite STF 15/180, Verder Scientific, Haan, Germany). For quenching, the samples were rapidly dropped into cold water. The annealing temperature was chosen based on our previous works [11,12] to obtain a homogeneous structure. After growth and quenching, the surface of single crystals was studied by SEM using TESCAN VEGA 3 (Tescan Group, Brno-Kohoutovice, Czech Republic). The chemical composition of $Ni_{44}Fe_{19}Ga_{27}Co_{10}$ and the homogeneous structure without admixtures were determined. The aging temperature was chosen for the precipitation of ω-phase particles [7,12]. The temperatures of the forward and reverse MT were determined by using the temperature dependence of the electrical resistance. An electro-mechanical testing frame (Instron VHS 5969, Instron, High Wycombe, UK) and an electro-dynamic testing

frame (ElectroPuls E3000, Instron, High Wycombe, UK) were used for cyclic tests under compressive load. The compression samples were parallelepipeds with dimensions of $3 \times 3 \times 6$ mm^3. Cyclic tests were performed at room temperature (295 K) during loading/unloading cycles up to a stress level of 300 MPa. The deformation rate for 1–10^5 cycles was V = $9.0 \times 10^{-2} \cdot$s^{-1}; for cycles above 10^5 the deformation rate was V = $21.0 \times 10^{-2} \cdot$s^{-1}. A Universal Keyence VHX 2000 complex (Keyence CORP, Itasca, IL, USA) with a Linkam TST350 testing frame (Redhill, Surrey RH1 5DZ, UK) for in situ compression was used for metallographic observations. A Hitachi HT-7700 electron microscope (Hitachi, Tokyo, Japan) was used for electron microscopy. For electron microscopy, the samples of 3 mm in diameter were mechanically thinned until 0.1 mm and polished using TenuPol-5 electrolytic thinning installation (Struers S.A.S., Champigny-sur-Marne, France).

3. Results

The microstructures of the quenched and aged single crystals are shown in Figure 1 and correspond to those reported in previous studies [11,12]. High-temperature annealing was conducted at 1448 K, above the order-disorder transition temperature [12], and led to the formation of a mixture of B2 and L2$_1$-structures.
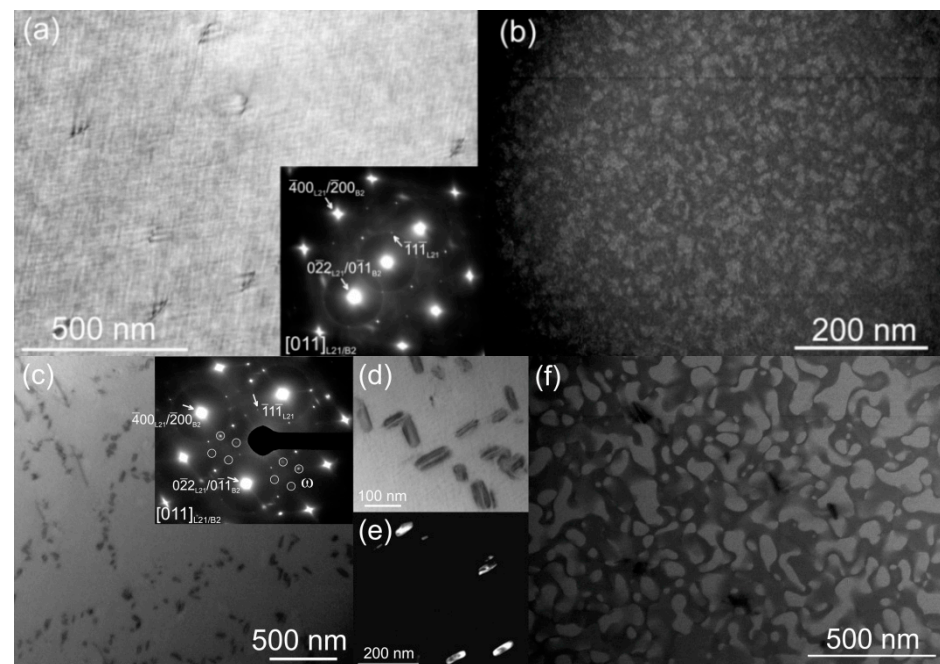

Figure 1. Microstructures of Ni$_{44}$Fe$_{19}$Ga$_{27}$Co$_{10}$ single crystals before cycling: (**a**,**b**) quenched crystals; (**c**–**f**) aged crystals; (**a**,**c**,**d**) bright-field images and SAEDPs with the [011]$_{L21/B2}$ zone axes of the matrix; (**b**,**f**) dark-field images in the <111>$_{L21}$ reflexes marked with arrows in the SAEDPs from (**a**,**c**); dark-field images contain some bright areas, they are L2$_1$-domains; (**e**) dark-field image in the circled reflex on SAEDP from (**c**) showing ω-phase particles.

Both the B2- and L2$_1$-structures have a bcc lattice. The difference between the L2$_1$-lattice and the B2-lattice lies in the ordered arrangement of Fe and Ga atoms at the sites of the sublattice and the lattice parameter [1]. In Figure 1a, the selected area electron diffraction patterns (SAEDPs) for the [011]$_{L2_1}$ and the [011]$_{B2}$ zone axes practically coincide. The lattice parameter of the B2 structure is two times smaller than the lattice parameter of the L2$_1$-structure $a_{L2_1} = 2 \cdot a_{B2}$; therefore, on SAEDP, $r_{hkl}^{L2_1} = 2 \cdot r_{hkl}^{B2}$, hence, the positions of the reflections $[\overline{4}00]_{L2_1}$ and $[\overline{2}00]_{L2_1}$ coincide. In quenched crystals, the mixture of B2 and L2$_1$-structures was visible as nanodomains of 20–50 nm on the dark-field images in the <111> reflections (Figure 1b). The volume fraction of the L2$_1$-structure derived from the dark-field images was estimated to be 40% in the quenched crystals. The fine tweed structure in

Figure 1a is typical for shape memory alloys and was observed in both quenched and aged single crystals.

Aging leads to the precipitation of disordered ω-phase particles with sizes of 70–100 nm and a volume fraction of 4–6% (Figure 1). The reflexes in positions 1/3 and 2/3 $[224]_{L21}$ on SAEDP (Figure 1c) confirm the ω-structure. The reflex in position 1/3 $[224]_{L21}$ corresponds to $[0001]_\omega$. Aging causes an increase in the size of the B2 and $L2_1$ phase domains of up to 100–200 nm (Figure 1b,f). The volume fraction of the $L2_1$-structure increases up to 60–65% in the aged crystals compared to the quenched ones. A more detailed description of the microstructure before testing is presented in [12].

The MT temperatures for the quenched crystals were M_s = 203 K, M_f = 163 K, A_s = 173 K, and A_f = 218 K. For the aged crystals, MT temperatures were M_s = 251 K, M_f = 217 K, A_s = 228 K, and A_f = 262 K. The MT temperatures in the aged single crystals were higher than those in the quenched ones, which is associated with the precipitation of particles rich in iron and cobalt. Particles led to decreases in the content of these elements in the matrix and an increase in the MT temperatures. In [12], more details are presented about the change in the MT temperatures after the precipitation of dispersed particles in these crystals.

Cyclic tests were performed at 295 K during loading/unloading cycles at stresses up to 300 MPa, sufficient for complete stress-induced MT in the quenched and aged single crystals (Figure 2). The σ(ε) curves are characterized by different critical stresses $σ_{cr}$, which are determined by different MT temperatures in accordance with the Clausius–Clapeyron equation. The higher the temperature M_s, the lower the critical stress $σ_{cr}$ at 295 K. The total strains were close, whereas the reversible strains determined at the $σ_{cr}$ differed in the quenched (3.8%) and aged (4.3%) crystals because of the higher stress for MT in the quenched crystals. A decrease in strain with an increase in stress was observed in all NiFeGaCo alloys and is associated with the difference in the elastic moduli of austenite and martensite, as well as with a change in the austenite lattice parameter before the start of MT [17,18].
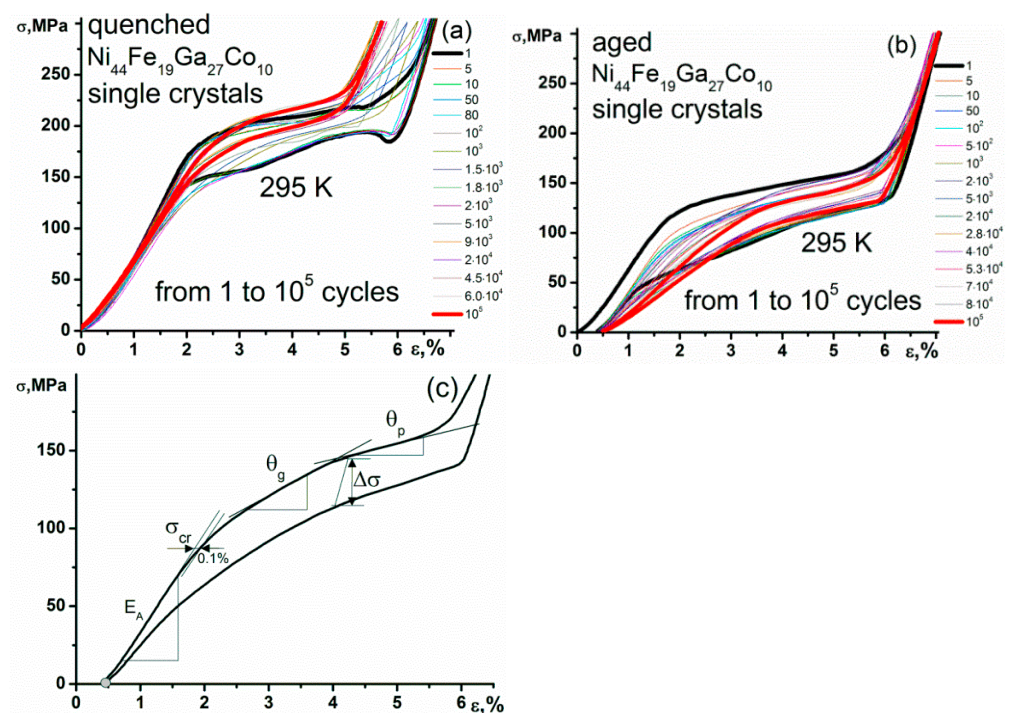

Figure 2. The σ(ε) response: (**a**) 1–10^5 cycles for quenched single crystals; (**b**) 1–10^5 cycles for aged single crystals; the bold black curve is the first cycle; the red curve is the last cycle; (**c**) schematic representation of the σ(ε) curve with measured parameters.

As shown in Figure 2, SE degradation (i.e., a change in the parameters of the $\sigma(\varepsilon)$ curves with an increased number of cycles) was observed in both quenched and aged crystals. The SE degrades in different ways depending on the microstructure. Figure 3 shows the dependence of the SE parameters on the number of cycles: the critical stress, σ_{cr}, the stress hysteresis, $\Delta\sigma$, the effective elastic modulus of austenite, E_A, and the strain hardening coefficient, $\theta = d\sigma/d\varepsilon$ (θ_P and θ_g). These parameters were determined, as shown in Figure 2c.

In Figure 3, the dependences of the SE parameters on the number of cycles in the quenched and aged crystals can be divided into three stages, typical of shape memory alloys [4–6,19–22]. The first stage of initial degradation was observed during the earliest cycles and was characterized by a sharp decrease in the critical stress, σ_{cr}, and the stress hysteresis, $\Delta\sigma$, and a change in the shape of the curves. The second stage of high stability was the longest, and σ_{cr} and $\Delta\sigma$ did not change. The third stage was cyclic fatigue, at which the SE parameters again underwent strong changes. The third stage was observed only in the aged crystals.
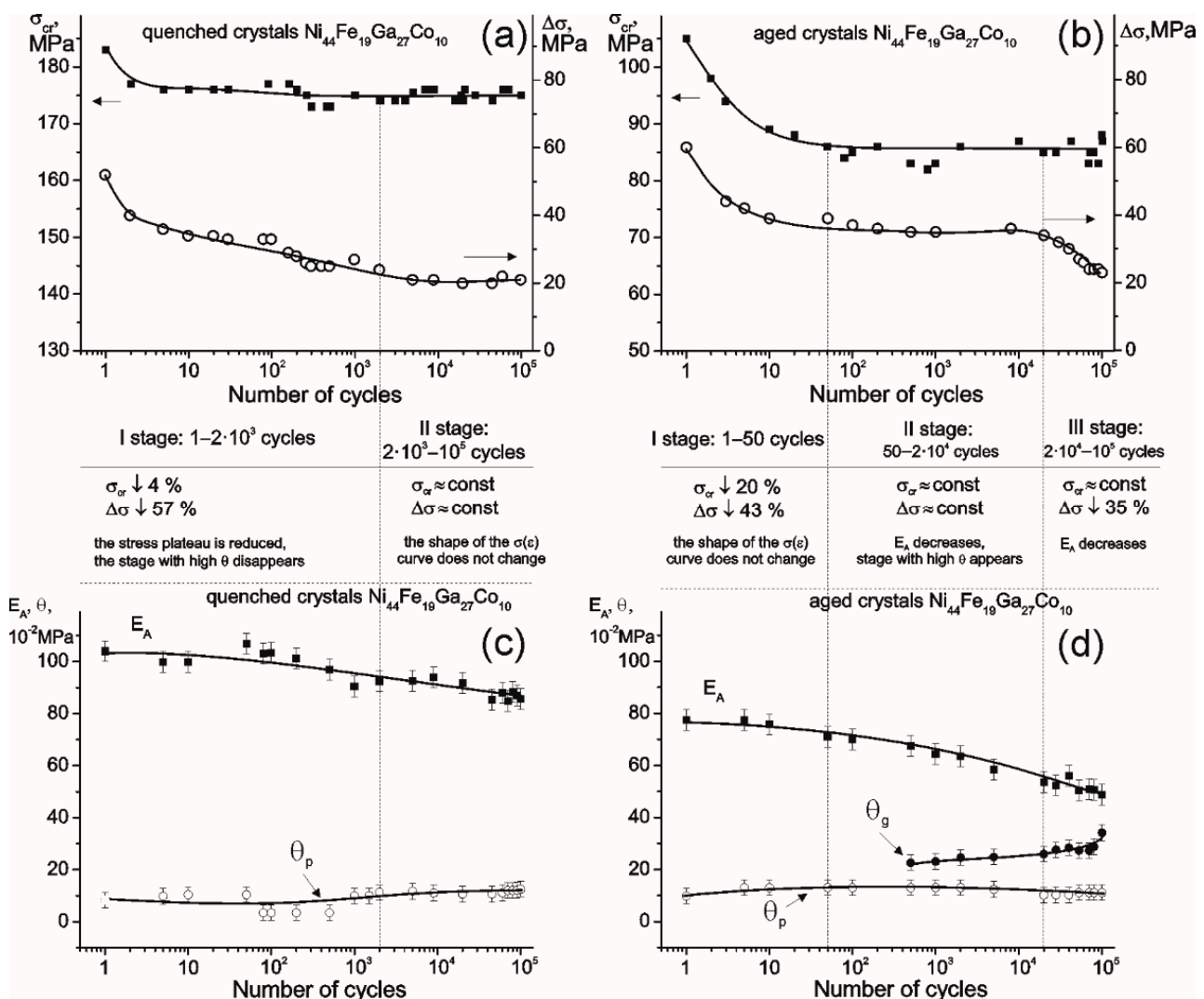

Figure 3. Dependence of critical stress, σ_{cr}, stress hysteresis, $\Delta\sigma$, strain hardening coefficient, $\theta = d\sigma/d\varepsilon$ (θ_p and θ_g), and elastic modulus of austenite, E_A, on the number of cycles (from 1 to 10^5): (**a**,**c**) quenched single crystals; (**b**,**d**) aged single crystals.

In the quenched single crystals, the first stage lasted from 1 to 2×10^3 cycles. In the first stage, σ_{cr} and $\Delta\sigma$ decreased by 4% and 57%, respectively. The $\sigma(\varepsilon)$ curves were

characterized by a stress plateau with a low strain hardening coefficient, $\theta_P = d\sigma/d\varepsilon$, close to zero. In this case, the shape of the $\sigma(\varepsilon)$ curve changed greatly. After the stress plateau, the $\sigma(\varepsilon)$ curve showed a segment with high $\theta = d\sigma/d\varepsilon$ and a wide hysteresis $\Delta\sigma$. With an increasing number of cycles, the coefficient $\theta = d\sigma/d\varepsilon$ increased, whereas the strain for a given segment decreased, reducing the hysteresis and the total reversible strain without the appearance of irreversibility. The reasons for the change in the form of the curve require further research. The second stage of high cyclic stability in the quenched single crystals was the longest and lasted from 2×10^3 to 1.2×10^5 cycles. In the second stage, the critical stress, σ_{cr}, the stress hysteresis, $\Delta\sigma$, and the effective elastic modulus of the austenite, E_A, almost did not change. The shape of the curve did not change during the second stage. The third stage was not reached in quenched crystals.

A different pattern of SE degradation was observed in the aged crystals. The first stage of the initial degradation was more than 10 times shorter than that of the quenched crystals and lasted from 1 to 50 cycles. In the first stage, a more noticeable decrease of 20% in the critical stress, σ_{cr}, was observed in the aged crystals, which was five times greater than in the quenched ones. The decrease in the hysteresis, $\Delta\sigma$, by 43% was comparable to the quenched crystals. The form of the $\sigma(\varepsilon)$ curve did not change. In aged single crystals, an irreversible strain of 0.5% was recorded during the first cycles.

The second stage of cyclic stability in the aged crystals was five times shorter than that of the quenched crystals and lasted from 50 to 2×10^4 cycles. The critical stress, σ_{cr}, and the stress hysteresis, $\Delta\sigma$, did not change during the second stage, but there was a significant change in the shape of the $\sigma(\varepsilon)$ curve: a significant decrease in the effective elastic modulus of austenite, E_A, by 25% and the appearance of segments in the $\sigma(\varepsilon)$ curves with different coefficients $\theta = d\sigma/d\varepsilon$. During the first cycles, the forward MT on the $\sigma(\varepsilon)$ curve takes one stage with a stress plateau; after 5×10^2 cycles, the forward MT takes two stages. After reaching the critical stress, a new segment with a high coefficient ($\theta_g = d\sigma/d\varepsilon \approx 20 \times 10^2$ MPa) appeared on the curve. A low-θ_p stress plateau followed the high-θ_g segment. When the number of cycles increased from 5×10^2 to 2×10^4, the coefficient θ_g increased by 25%, while the coefficient $\theta_p = d\sigma/d\varepsilon$ on the stress plateau remained constant.

In aged crystals, a third stage of cyclic fatigue was observed after 2×10^4 cycles. The critical stress changed little at this stage, but the hysteresis was significantly reduced by 35% compared to the second stage. The shape of the curve continued to change. The elastic modulus, E_A, decreased by 11%. The segment of the curve with high-$\theta_g = d\sigma/d\varepsilon$ decreased in the strain by almost two times, while $\theta_g = d\sigma/d\varepsilon$ increased by 35% compared to the second stage of cyclic stability (Figure 3d). A similar change in the SE parameters was also observed in aged $Ni_{49}Fe_{18}Ga_{27}Co_6$ single crystals [6].

4. Discussion

The presence of ω-phase particles was the main reason for the changes in the degradation processes and cyclic stability during the transition from quenched to aged $Ni_{44}Fe_{19}Ga_{27}Co_{10}$ single crystals. First, the particles are quite large, up to 70–100 nm; therefore, they could partially lose coherence with the matrix. In this case, the particles act as stress concentrators and places for dislocation accumulation and can be nucleation sites for non-oriented martensite. Second, these particles led to a decrease in the cobalt content in the matrix, which reduces the brittleness typical of NiFeGaCo alloys with high cobalt content [7–9]. The difference in the resistance to cyclic tests in single crystals with various cobalt contents has been researched in [11]. We have studied the SE in quenched $Ni_{44}Fe_{19}Ga_{27}Co_{10}$ and $Ni_{39}Fe_{19}Ga_{27}Co_{15}$ single crystals and found that high cobalt content results in strong degradation of the SE at the first stage and destruction of the samples within 30–50 cycles [11].

It should be noted that the $B2 + L2_1$ nanodomain structure also has a significant effect on thermal- and stress-induced MTs. In [12], authors considered two microstructures in $Ni_{44}Fe_{19}Ga_{27}Co_{10}$ single crystals: as-grown single crystals, where there is no nanodomain structure and the high-temperature phase is $L2_1$-austenite, and quenched single crystals

with a nanodomain (B2 + L2$_1$)-microstructure, as in the present work. It has been shown that for the microstructure containing nanodomains, the stored elastic energy ΔG_{rev} during MT upon cooling/heating is 5–8 times greater than for a single L2$_1$-structure. The stored elastic energy ΔG_{rev} can be estimated from the temperature intervals of the thermal-induced MT [23]. The elastic energy ΔG_{rev} remained high even after aging due to the nanodomain structure (only the size of the domains changed). The high level of stored elastic energy during MT determines the high cyclic stability observed in both the quenched and aged single crystals. As can be seen from the experimental data, the quenched and aged single crystals withstood more than 10^5 cycles without destruction. However, they demonstrated different degradation mechanisms owing to their different microstructural parameters. The ω-phase particles determined the differences in the features of the SE cyclic stability at each stage.

4.1. First Stage of Initial Degradation

In the initial degradation stage in quenched and aged Ni$_{44}$Fe$_{19}$Ga$_{27}$Co$_{10}$ single crystals, the elastic stresses relaxed near the austenite/martensite interface due to the formation of dislocations, residual martensite, and martensite stabilization [4−6,19−22]. In this case, in each subsequent cycle, martensite will be nucleated on the defects remaining after the previous cycle. This facilitates the nucleation of stress martensite and leads to a decrease in critical stress.

In the quenched crystals, the change in critical stress at the first stage of degradation was small, only 4%, whereas, in the aged crystals, the decrease in stress was five times greater. This suggests that the volume fraction of residual martensite and the number of defects were greater in the aged crystals than in the quenched crystals. Indeed, the $\sigma(\varepsilon)$ curves in the first stage of the initial degradation showed an irreversible strain of 0.5% in the aged crystals, in contrast to the quenched crystals without irreversible strain. Notably, the number of cycles at the first stage of degradation in the aged crystals was 10 times less. Thus, more intensive degradation occurred in the aged crystals in fewer cycles than in the quenched crystals.

4.2. Second Stage of High Cyclic Stability

The second stage (Figure 3) was characterized by high stability in the quenched and aged crystals. This stage was five times shorter for the aged single crystals than for the quenched crystals. Although the level of critical stress, σ_{cr}, and the stress hysteresis, $\Delta\sigma$, practically did not change, the shape of the curves changed significantly during the second stage in the aged crystals. There was a decrease in the elastic modulus of austenite E_A; an additional segment appears on the curve with a high coefficient θ_g.

The observed change in the elastic modulus of austenite with an increase in the number of cycles above 5×10^2 in the aged single crystals can be associated with the following processes. First, the microstructure of the aged single crystals changed, and defects and residual martensite appeared. This microstructure differs from defect-free austenite, which was subjected to elastic deformation during the first loading/unloading cycle. Therefore, a mixture of austenite and residual martensite with a high content of stress concentrators (dislocations, residual martensite, and ω-phase particles) is subjected to elastic deformation. Second, stress concentrators are the sites of martensite nucleation. As shown in [24], the stress concentration regions could locally eliminate the nucleation barrier and thus induce equilibrium nanosized embryos of martensite. Consequently, martensite nuclei can appear at a stress below the critical stress, σ_{cr}. This assumption was confirmed by optical observations of the surface of the aged single crystals after 2×10^3 loading/unloading cycles (Figure 4). Without the applied stress, residual martensite was observed in these samples (Figure 4a). As the compressive load increased to small values of 21–63 MPa < σ_{cr}, the residual martensite crystals increased in size, and new stress-induced martensite crystals grew from them.

As shown in Figure 4a, the martensite variants had different orientations. The appearance of non-oriented martensite variants could be caused by the internal stress fields from particles, dislocations, and residual martensite. Following the Clausius–Clapeyron equation, these internal stress fields led to a local increase in the temperature of nucleation of the thermal-induced martensite. For $Ni_{44}Fe_{19}Ga_{27}Co_{10}$ alloys, the coefficient describing the increase in the temperature, M_s^σ, with increasing stress is very low and equals 1.2–1.3 MPa/K [11]. In other words, small internal stresses can significantly shift the temperature of thermal-induced martensite. Then, the martensite observed in Figure 4a may be partly residual and partly thermal-induced, appearing due to the internal stress fields. Indeed, the branched structure of different orientations, as shown in Figure 4a, is characteristic of thermal-induced martensite. If the applied stress increases, this martensite can interact with oriented stress-induced martensite crystals that arise at σ_{cr} and higher. The variant–variant interaction led to an additional segment on the curve with a high coefficient θ_g, which was observed in the aged crystals after 10^3 cycles (Figures 2–4). The additional segment on the curve was related to MT in the part of the sample that has undergone the most plastic deformation, namely, in the part where the greatest number of defects and residual martensite were contained. After the completion of the MT in this region, the transformation occurred in the regions that were less exposed to plastic deformation. This process was accompanied by a stress plateau on the $\sigma(\varepsilon)$ curve. The variant–variant interaction played a more important role in increasing the number of cycles caused by the growth of dislocations and volume fraction of residual martensite. This led to an increase in coefficient θ_g at the second and third stages (Figure 2d).
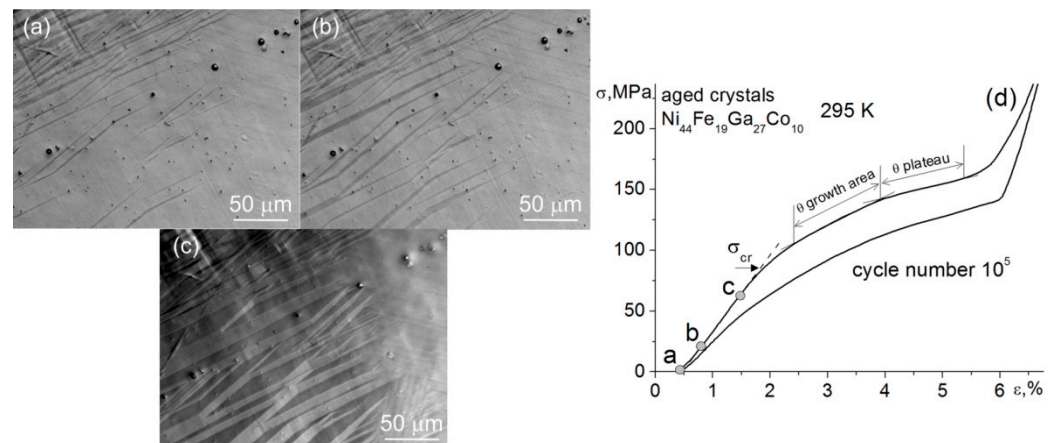

Figure 4. In situ compressive loading for aged $Ni_{44}Fe_{19}Ga_{27}Co_{10}$ single crystals: (**a–c**) optical metallography of the surface during in situ compressive loading from 0 to 63 MPa; (**d**) $\sigma(\varepsilon)$ curve at cycle number 2×10^3 at 295 K.

4.3. Third Stage of Cyclic Fatigue and Changes in the Microstructure after Cycling

The quenched single crystals did not reach the third stage of cyclic fatigue within 10^5 cycles. Additional tests showed that the quenched single crystals underwent brittle fracture after 1.2×10^5 cycles without significantly changing the SE parameters. In contrast, after 2×10^4 cycles, the aged single crystals showed the third stage of cyclic fatigue and failed after 1.7×10^5 cycles. In this case, the stress hysteresis, $\Delta\sigma$, the elastic modulus of austenite, E_A, and the coefficient θ_g changed significantly with the number of cycles (Figure 3). These changes are correlated. The decrease in the elastic modulus of austenite, E_A, and the increase in the high-θ_g segment of the curves strongly reduced the low-θ_p stress plateau. The decrease in transformation strain at the low-θ_p stress plateau led to the decrease in stress hysteresis because the smaller volume fraction of the matrix underwent the MT, increasing the number of cycles. A similar stage of cyclic fatigue has also been observed in aged single crystals with a lower cobalt content, $Ni_{49}Fe_{18}Ga_{27}Co_6$ (at.%), after 2×10^4 cycles [6]. The aged $Ni_{49}Fe_{18}Ga_{27}Co_6$ single crystals contained

γ'-phase fine particles smaller than 30 nm and large γ-phase particles of size $5-15$ µm, which deformed during testing. The observed dependence of the SE parameters on the number of cycles may be a general property of NiFeGaCo single crystals containing secondary phase particles.

Figures 5 and 6 show the electron microscopy of the quenched and aged single crystals after 10^5 loading/unloading cycles. The degradation of the microstructure in the quenched and aged single crystals proceeded in different ways. First, a higher density of dislocations (Figure 6a) occurred in the aged single crystals than in the quenched ones; the particles served as places for dislocations accumulation (Figure 6b), and residual martensite was observed (Figure 6c). Residual martensite was not found in the quenched crystals using either optical or electron microscopy. It should be mentioned that the difficulties with the pinning and stabilization of martensite are typical for strain glass alloys and were faced frequently in TiNi strain glass alloys. It can also be revealed in quenched $Ni_{44}Fe_{19}Ga_{27}Co_{10}$ single crystals because of high cobalt content and vicinity to the strain glass composition. In contrast, in aged single crystals with second phase particles reducing the cobalt content, martensite is easily pinned by dislocations and particles.
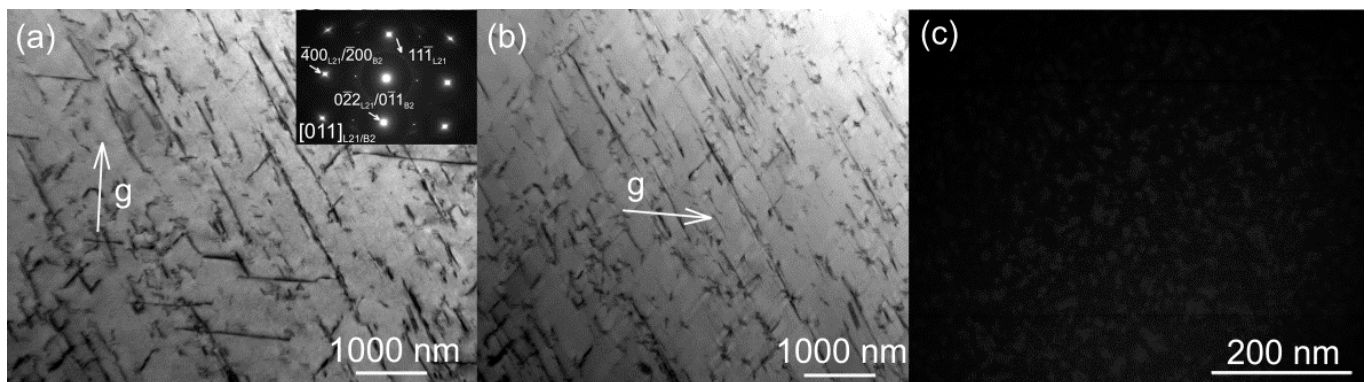

Figure 5. Microstructure of quenched $Ni_{44}Fe_{19}Ga_{27}Co_{10}$ single crystals after cycling: (**a**,**b**) bright-field images and SAEDPs with the $[011]_{L21/B2}$ zone axis of the matrix; (**c**) dark-field image in the $<111>_{L21}$ reflex marked with an arrow in the SAEDP.

Second, no interaction between the nanodomain structure and dislocations was observed in the quenched crystals (Figure 5c), unlike in the aged crystals (Figure 6d). A separation of the nanodomains of the austenitic $L2_1$-structure was observed in the aged single crystals. From experimental studies [25], the slip systems in Ni_2FeGa austenite are likely to be (011)<111> and (011)<001>. In this case, the (011)<111> system is preferable because it is characterized by a lower energy barrier and low activation stress. The slip for this system for the B2 structure would consist of two superpartial dislocations connected by two nearest-neighbor and next-nearest-neighbor antiphase nanodomain boundaries [26]. Refs. [27,28] considered the case where the edge superpartial dislocation pair glided on a slip plane across an antiphase nanodomain boundary perpendicular to the Burgers vector. When the leading superpartial dislocation penetrates the antiphase nanodomain boundary under the influence of the applied stress, a thin band of perfect crystal forms [27,28]. The cases in Figure 6d occurred where the trailing superpartial dislocation had not yet reached the position of the antiphase nanodomain boundary. When the trailing superpartial dislocation met the antiphase nanodomain boundary, further forward motion required the creation of an additional area of the antiphase nanodomain as the dislocation crossed the band of the perfect crystal.
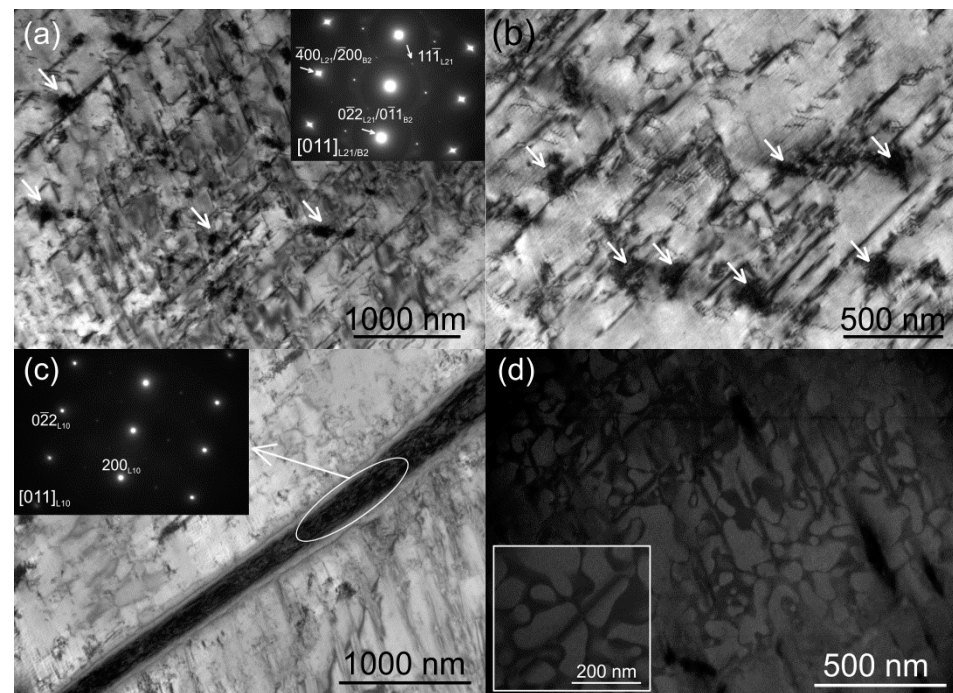
Figure 6. Microstructure of aged $Ni_{44}Fe_{19}Ga_{27}Co_{10}$ single crystals after cycling: (**a,b**) bright-field images and SAEDPs with the $[011]_{L21/B2}$ zone axes of the matrix, ω-particles marked with arrows; (**c**) bright-field image with $L1_0$-martensite lamella, $[011]_{L10}$ zone axis of the martensite; (**d**) dark-field image in the $<111>_{L21}$ reflex marked with an arrow in the SAEDP from (**a**), dark-field image showing bright $L2_1$-domains with tracks from the dislocation motion.

It can be concluded from the foregoing that SE degradation occurs differently in quenched and aged single crystals. In quenched crystals, the main degradation mechanism is the formation of a uniform distribution of dislocations (Figure 7). In aged single crystals, the degradation mechanism differs and consists of a non-uniform distribution of dislocations around the particles and the appearance of residual martensite. The ω-phase particles play the main role in aged crystals. These particles serve as additional stress concentrators and reduce the cobalt content, embrittling the matrix. There were a large number of defects and residual martensite fixed around the particles (Figure 7). Therefore, in aged single crystals, the relaxation of elastic stresses during cyclic tests was more active than in quenched crystals, as evidenced by the more significant change in the SE parameters over a smaller number of cycles (Figures 2 and 3). In contrast, the quenched crystals contain smaller stress concentrators that contribute to the relaxation of elastic stresses. As a result, locally high stresses that did not relax led to sample destruction without the third stage of degradation.
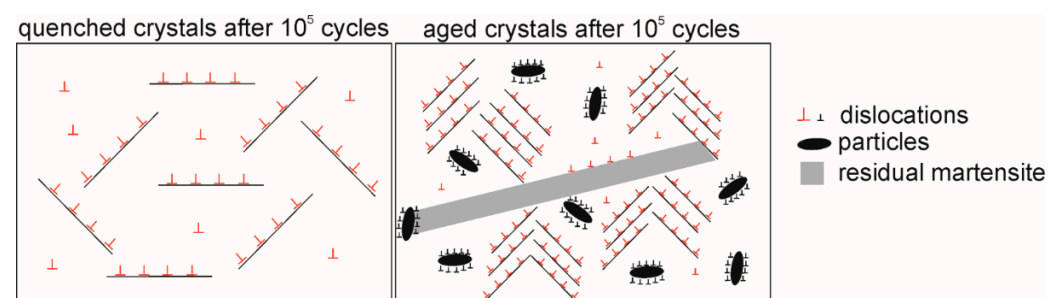

Figure 7. Scheme of microstructures of aged and quenched $Ni_{44}Fe_{19}Ga_{27}Co_{10}$ single crystals after cycling.

5. Conclusions

It was experimentally established that quenched and aged $Ni_{44}Fe_{19}Ga_{27}Co_{10}$ single crystals (at.%) withstood 10^5 loading/unloading cycles of SE at 295 K without breaking, which makes it promising for applications.

For the quenched crystals (quenched after annealing at 1448 K for 1 h), the degradation process of SE consisted of two stages: the first stage of the initial degradation with a significant decrease in the SE parameters and the second stage of high cyclic stability and small parameters change. The main degradation mechanism was the formation of a uniform distribution of dislocations.

Aging at 773 K for 1 h caused the precipitation of particles of the ω-phase with a size of 70–100 nm, which led to the change of both the degradation process of SE and the microstructural degradation mechanisms. The degradation process was more intensive and occurred in smaller number of cycles with an additional cyclic fatigue stage, where SE parameters decreased sharply. The microstructural degradation mechanisms consist not only of a non-uniform distribution of dislocations but also include accumulation of the dislocations around the particles, which can contribute to pinning the residual martensite.

Author Contributions: Conceptualization, E.T., E.P. and Y.I.C.; methodology, Y.I.C.; validation, A.T. and M.Z.; formal analysis, E.P. and E.T.; investigation, M.Z.; resources, A.T. and M.Z.; writing—original draft preparation, E.T.; writing—review and editing, E.P., E.T. and Y.I.C.; visualization, E.T.; supervision, E.P. and Y.I.C.; project administration, E.T. All authors have read and agreed to the published version of the manuscript.

Data Availability Statement: The data used in this article are presented in the manuscript.

Conflicts of Interest: The authors declare no conflict of interest.

References

1. Hamilton, R.; Sehitoglu, H.; Efstathiou, C.; Maier, H. Inter-martensitic transitions in Ni–Fe–Ga single crystals. *Acta Mater.* **2007**, *55*, 4867. [CrossRef]
2. Masdeu, F.; Pons, J.; Torrens-Serra, J.; Chumlyakov, Y.; Cesari, E. Superelastic behavior and elastocaloric effect in a $Ni_{51.5}Fe_{21.5}Ga_{27.0}$ ferromagnetic shape memory single crystal under compression. *Mater. Sci. Eng. A* **2022**, *833*, 142362. [CrossRef]
3. Masdeu, F.; Pons, J.; Chumlyakov, Y.; Cesari, E. Two-way shape memory effect in $Ni_{49}Fe_{18}Ga_{27}Co_6$ ferromagnetic shape memory single crystals. *Mater. Sci. Eng. A* **2021**, *805*, 140543. [CrossRef]
4. Efstathiou, C.; Sehitoglu, H.; Kurath, P.; Foletti, S.; Davoli, P. Fatigue response of NiFeGa single crystals. *Scr. Mater.* **2007**, *57*, 409–412. [CrossRef]
5. Imran, M.; Zhang, X. Recent developments on the cyclic stability in elastocaloric materials. *Mater. Des.* **2020**, *195*, 109030. [CrossRef]
6. Larchenkova, N.; Panchenko, E.; Timofeeva, E.; Tagiltsev, A.; Chumlyakov, Y. Cyclic stability of superelasticity in [001]-oriented stress-free and stress-assisted aged $Ni_{49}Fe_{18}Ga_{27}Co_6$ single crystals. *AIP Conf. Proc.* **2008**, *2051*, 020166.
7. Chen, H.; Wang, Y.; Nie, Z.; Li, R.; Cong, D.; Liu, W.; Ye, F.; Liu, Y.; Cao, P.; Tian, F.; et al. Unprecedented non-hysteretic superelasticity of [001]-oriented NiCoFeGa single crystals. *Nat. Mater.* **2020**, *19*, 712–718. [CrossRef]
8. Zhang, Q.; Zhai, Z.; Nie, Z.; Harjo, S.; Cong, D.; Wang, M.; Lie, J.; Wang, Y. An in situ neutron diffraction study of anomalous superelasticity in a strain glass $Ni_{43}Fe_{18}Ga_{27}Co_{12}$ alloy. *J. Appl. Crystallogr.* **2015**, *48*, 1183. [CrossRef]
9. Sun, X.; Cong, D.; Ren, Y.; Liss, K.-D.; Brown, D.E.; Ma, Z.; Hao, S.; Xia, W.; Chen, Z.; Ma, L.; et al. Magnetic-field-induced strain-glass-to-martensite transition in a Fe-Mn-Ga alloy. *Acta Mater.* **2020**, *183*, 11–23. [CrossRef]
10. Hao, C.; Wang, Y.; Wu, X.; Guo, Y.; Liu, C.; He, L.; Adil, M.; Yang, S.; Song, X. High performance damping behavior of Ni-Fe-Ga alloys within the martensite/strain-glass phase boundary. *J. Alloys Compd.* **2022**, *898*, 162954. [CrossRef]
11. Timofeeva, E.; Panchenko, E.; Eftifeeva, A.; Tagiltsev, A.; Surikov, N.; Tokhmetova, A.; Yanushonite, E.; Zherdeva, M.; Karaman, I.; Chumlyakov, Y. Cyclic stability of superelasticity in [001]-oriented quenched $Ni_{44}Fe_{19}Ga_{27}Co_{10}$ and $Ni_{39}Fe_{19}Ga_{27}Co_{15}$ single crystals. *Acta Metall. Sin.* **2023**, *36*, 650–660. [CrossRef]
12. Timofeeva, E.; Panchenko, E.; Zherdeva, M.; Tokhmetova, A.; Surikov, N.; Chumlyakov, Y.; Karaman, I. The effect of thermal treatment on microstructure and thermal-induced martensitic transformations in $Ni_{44}Fe_{19}Ga_{27}Co_{10}$ single crystals. *Metals* **2022**, *12*, 1960. [CrossRef]

13. Timofeeva, E.E.; Panchenko, E.Y.; Zherdeva, M.V.; Chumlyakov, Y.I.; Karaman, I. Thermal- and stress-induced martensitic transformations in [001]-oriented $Ni_{44}Fe_{19}Ga_{27}Co_{10}$ single crystals. *Mater. Lett.* **2022**, *310*, 131477. [CrossRef]
14. Hornbogen, E. Review Thermo-mechanical fatigue of shape memory alloys. *J. Mater. Sci.* **2004**, *39*, 385–399. [CrossRef]
15. Dutta, P.S. Bulk growth of crystals of III–V compound semiconductors. *Semicond. Sci. Technol.* **2011**, *3*, 36–80.
16. Venkataraman, R. Semiconductor detectors. In *Handbook of Radioactivity Analysis*, 4th ed.; L'Annunziata, M.F., Ed.; Academic Press: Cambridge, MA, USA, 2020; Volume 1, pp. 409–491.
17. Ding, X.D.; Suzuki, T.; Suna, J.; Ren, X.; Otsuka, K. Study on elastic constant softening in stress-induced martensitic transformation by molecular dynamics simulation. *Mater. Sci. Eng. A* **2006**, *438–440*, 113–117. [CrossRef]
18. Lauhoff, C.; Reul, A.; Langenkämper, D.; Krooß, P.; Somsen, C.; Gutmann, M.; Pedersen, B.; Kireeva, I.; Chumlyakov, Y.; Eggeler, G.; et al. Effects of aging on the stress-induced martensitic transformation and cyclic superelastic properties in Co-Ni-Ga shape memory alloy single crystals under compression. *Acta Mater.* **2022**, *226*, 117623. [CrossRef]
19. Li, X.; Chen, H.; Guo, W.; Guan, Y.; Wang, Z.; Zeng, Q.; Wang, X. Improved superelastic stability of NiTi shape memory alloys through surface nano-crystallization followed by low temperature aging treatment. *Intermetallics* **2021**, *131*, 107114. [CrossRef]
20. Gall, K.; Maier, H. Cyclic deformation mechanisms in precipitated NiTi shape memory alloys. *Acta Mater.* **2002**, *50*, 4643–4657. [CrossRef]
21. Krooß, P.; Kadletz, P.; Somsen, C.; Gutmann, M.; Chumlyakov, Y.; Schmahl, W.; Maier, H.; Niendorf, T. Cyclic degradation of $Co_{49}Ni_{21}Ga_{30}$ high-temperature shape memory alloy: On the roles of dislocation activity and chemical order. *Shape Mem. Superelast.* **2016**, *2*, 37–49. [CrossRef]
22. Kann, Q.; Yu, C.; Kang, G.; Li, J.; Yan, W. Experimental observations on rate-dependent cyclic deformation of superelastic NiTi shape memory alloy. *Mech. Mater.* **2016**, *97*, 48–58. [CrossRef]
23. Beke, D.; Daróczi, L.; Samy, N.; Tóth, L.; Bolgár, M. On the thermodynamic analysis of martensite stabilization treatments. *Acta Mater.* **2020**, *200*, 490–501. [CrossRef]
24. Rao, W.; Xu, Y.; Hu, C.; Khachaturyan, A. Magnetoelastic equilibrium and super-magnetostriction in highly defected pre-transitional materials. *Acta Mater.* **2020**, *188*, 539–550. [CrossRef]
25. Sehitoglu, H.; Wang, J.; Maier, H. Transformation and slip behavior of Ni_2FeGa. *Int. J. Plast.* **2012**, *39*, 61–74. [CrossRef]
26. Chowdhury, P.; Sehitoglu, H. A revisit to atomistic rationale for slip in shape memory alloys. *Prog. Mater. Sci.* **2017**, *85*, 1–42. [CrossRef]
27. Koizumi, Y.; Minamino, Y.; Nakano, T.; Umakoshi, Y. Effects of antiphase domains on dislocation motion in Ti_3Al single crystals deformed by prism slip. *Philos. Mag.* **2008**, *88*, 465–468. [CrossRef]
28. Rong, T.; Aindow, M.; Jones, I. The interaction between extended dislocations and antiphase domain boundaries—I: Superpartial separation and the yield stress. *Intermetallics* **2001**, *9*, 499–506. [CrossRef]